Electric Field and Thermal Analysis of 132 kV Ceramic Oil-filled Cable Sealing Ends

Christos Zachariades, Vidyadhar Peesapati, *Member, IEEE,* Richard Gardner, Oliver Cwikowski

Abstract— **This paper reports on a method combining the use of finite element simulations and external measurements to provide preliminary condition diagnosis of oil-filled cable sealing ends (CSEs) without requiring downtime. Good agreement has been obtained between the predictions from the electric field and thermal simulations and the measurements on a 132 kV oil-filled CSE. The electrostatic computation combined with electric field measurements can provide information regarding the electric field distribution inside the CSE and help in identifying potential issues with the CSE design, the materials or the cable termination process. The thermal computation combined with thermal imaging can reveal potential problems, such as high resistance connection to the busbar, and provide information regarding the cooling efficiency of the liquid dielectric. The method presented can provide the starting point for prioritizing maintenance operations on CSEs.**

Index Terms— **cable sealing end (CSE), cable termination, condition monitoring, electric field, finite element analysis (FEA), simulation, thermal imaging.**

I. INTRODUCTION

Cable systems have a wide range of potential degradation modes. Failures can occur due to poor quality or ageing of the insulation or accessories [1, 2]. Insulation related degradation can include the existence of voids within the bulk of the insulation, the presence of contaminants, the existence of protrusions from the semiconducting screen, and even the incorrect dimensions of the cable [3]. Operation of the cable system under abnormal conditions can also cause failure [4]. This can be a result of system protection failure, incorrect determination of ampacity, or a lack of thermal backfill in the cable trench [5]. All these issues can potentially cause the cable to overheat and the insulation to become brittle and eventually crack [6]. Cables can also fail as a result of mechanical damage which can be caused either during installation, maintenance or by other external factors. Another frequent reason for cable failure is poor workmanship or improper installation of the cable and its components.

Cable accessories, such as cable terminations and joints, have a significant impact to the reliability of transmission systems mainly to the longer repair time of cable connections when

compared to overhead lines [7, 8]. Of particular interest are the fluid-filled terminations, also known as cable sealing ends (CSEs), used to facilitate the connection between a cable and other electrical equipment. They are constructed by fitting a stress cone on a prepared cable end. The cable end is then housed within an insulator, which can be either made out of porcelain or a composite material. The housing is filled with insulating oil, usually leaving a small volume empty to allow for expansion [9]. Although the failure rates of fluid-filled CSEs compared to other accessories is relatively low [10], explosive failures have been reported in the past [11] which have prompted development of solutions to minimize the potential risks to personnel and equipment [12].

The modes leading to failure of the CSEs are still under investigation. Generally, cable accessories, such as CSEs, are potential hot spots in cable circuits therefore temperature related effects are likely to be involved [13, 14]. The effect of increased heating due to increased harmonic levels from power electronic converters has also been investigated [15]. Other studies have focused on examining the quality of the oil used to fill the CSEs. They have shown that the evolution of gases from the oil could increase the risk of internal flashover [16]. Additionally, the ingress of water due to defective O-rings has been theorized to be a problem [11, 17].

With thousands of high voltage oil-filled CSEs in service in the United Kingdom, some of them several decades old, it is important to understand how the CSEs behave under operating and abnormal conditions. However, to formulate a holistic view, examination of the components and materials inside the CSE housing is required. This can be problematic since appropriate instrumentation including internal sensors is usually not pre-installed, and the CSEs are usually designed as 'seal-for-life' units. Furthermore, retrofitting sensors can be costly and time-consuming making replacement the most cost-effective asset management decision.

This paper presents a simulation methodology which can be used to examine the electric field distribution and the thermal performance oil-filled CSEs, using a 132 kV oil-filled CSE as an example. The electrostatic computation examines the electric field distribution and can pinpoint the areas where the highest electric field magnitude is observed. The thermal computation examines how the temperature of the CSE components changes as a result of Joule losses in the conductor. Different heat transfer modes are considered, specifically conduction and radiation. Also, the addition of computational fluid dynamics allows convection to be included, to take into account the movement of oil and air inside the CSE. In addition to the simulations, electric field and temperature measurements on the outside of two CSEs were performed. The aim was to
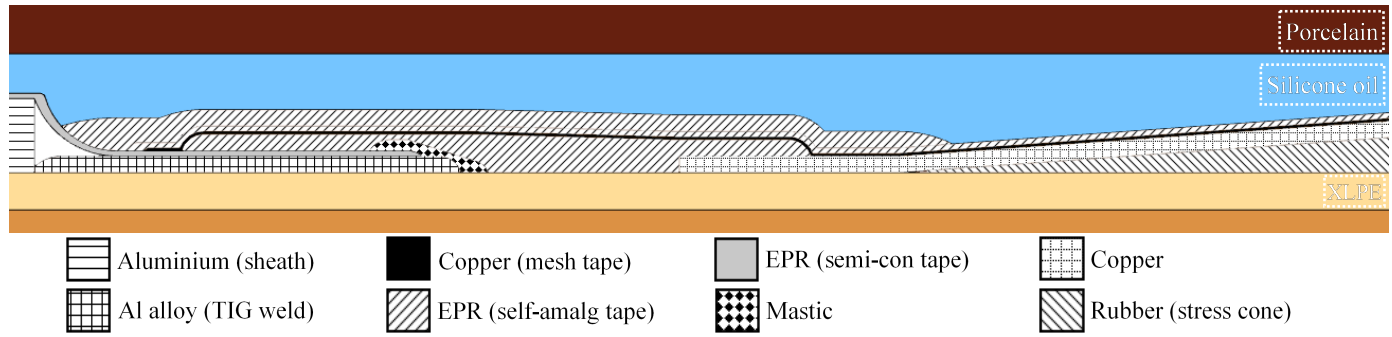
Fig. 1. Cross-section of the CSE model (not to scale) at the vicinity of the cable sheath termination showing the construction of the termination and the materials.

investigate whether external instrumentation combined with the simulation results can be used to diagnose the condition of a CSE without downtime.

II. SIMULATION METHODOLOGY

A high fidelity, three-dimensional (3D) model of the 132 kV CSE was reconstructed in a Computer Aided Design (CAD) software package using the original mechanical drawings which date back to 1985. Furthermore, an ex-service CSE was dismantled and the dimensions measured to verify the accuracy of the geometry. The model incorporated the majority of the constituent components of the CSE. These included the conductor, insulation and sheath of the cable, the stress cone, the porcelain housing, the grading rings as well as the several tapes (insulating, semiconducting and metallic) used in the termination of the cable (Fig. 1). Some minor components of the CSE were omitted from the model, such as nuts and bolts, base plates, and support structures, because their impact on the accuracy of the computations would be minimal.

A. Electric Field Simulation

The CSE is normally connected to a 50/60 Hz AC supply. Although the electric field is changing with time, the frequency is relatively low and therefore the field can be treated as electrostatic. By combining the definition of the electric potential under static conditions (1) with the constitutive relationship between the dielectric displacement and the electric field (2), the electrostatic field in dielectric materials can be described by equation (3) which is another form of Gauss' law:

$$\mathbf{E} = -\nabla V \tag{1}$$

$$\mathbf{D} = \varepsilon_0 \mathbf{E} + \mathbf{P} \tag{2}$$

$$-\nabla \cdot \left(\varepsilon_0 \nabla V - \mathbf{P} \right) = \rho \tag{3}$$

where $\mathbf{E}$ is the electric field, V is the electric potential, $\mathbf{D}$ is the electric displacement, $\mathbf{P}$ is the electric polarization vector, ε_0 is the permittivity of free space, and ρ is the charge density.

Equation (3) is used by the *Electrostatics* physics interface in the AC/DC module of COMSOL Multiphysics [18] which was used to perform the electric field computation. Since the CSE components comprise of linear isotropic materials, the polarization is:

$$\mathbf{P} = \varepsilon_0 \chi_e \mathbf{E} \tag{4}$$

where χ_e is the electric susceptibility which is related to the permittivity of a material, ε_r, as follows:

$$\varepsilon_r = \chi_e + 1 \tag{5}$$

Hence, the constitutive equation (2) can be expressed as:

$$\mathbf{D} = \varepsilon_0 \varepsilon_r \mathbf{E} \tag{6}$$

From (6) it can be observed that the only material property required for the electrostatic field computation is the permittivity. A list of the material permittivities used for the computation is given in Table I.

The electrically conducting parts of the model were assumed to be perfect conductors for which the Dirichlet boundary condition applies:

$$V = V_0 \tag{7}$$

where V_0 is a constant.

On all other boundaries, the Neumann boundary condition applies:

$$\frac{dV}{dn} = 0 \tag{8}$$

where n is the direction normal to the boundary.

In order to make the computation manageable in terms of memory requirements, simulation space was contained by placing the CSE model inside a cylindrical domain with a height of 2.4 m and a diameter of 1.0 m (Fig. 2). To avoid interference of this artificial domain with the correct computation of the electric field, an *Infinite Element Domain (IED)* node was used. The *IED* applies coordinate scaling to a layer of domains surrounding the encapsulating cylindrical domain so that it behaves as if it extends to infinity. The thickness of the *IED* layer was set to 0.1 m.

TABLE I
MATERIAL PROPERTIES FOR ELECTRIC FIELD COMPUTATION

| Component	Material	Relative permittivity
Enclosing domain	Air	1.0
Top and bottom rings	Brass	1.0
Outer shell	Porcelain	6.0
Bonding between rings and shell	Cement	2.5
Liquid dielectric	Silicone oil	2.7
Stress cone	Silicone rubber	2.6
Conductor and metallic tapes	Copper	1.0
Cable insulation	XLPE	2.3
Cable sheath and conductor stalk	Aluminum	1.0
TIG weld	Aluminum alloy	1.0
Semi-con tape	EPR	20
Self-amalgamating tape	EPR	3.0
Heat shrink	Rubber	2.3
Sealant	Mastic	7.0
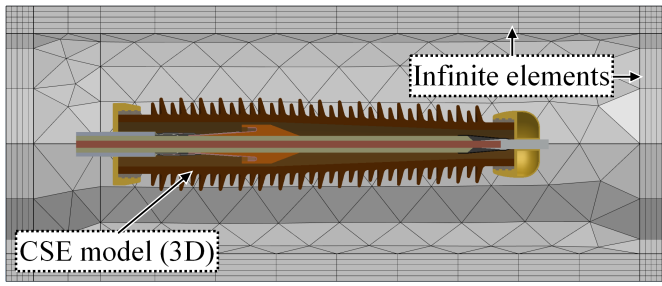
Fig. 2. Meshed computation space for the electric field computation containing the three-dimensional CSE model (cross-section shown), and demonstrating the use of the infinite elements domains at the outer edges of the encapsulating domain.

B. Thermal Simulation

Determining the thermal behavior of the CSE is more complicated compared to the determination of the electric field distribution. The CSE comprises of both solid and liquid materials which behave differently as their temperature changes. Hence, the *Heat Transfer in Solids and Fluids* physics interface in COMSOL Multiphysics [19] was used for the thermal analysis. Since heat transfer in solids is predominantly attributed to conduction, this interface solves equation (9), assuming isotropic materials:

$$\rho C_p \frac{\partial T}{\partial t} = \nabla \cdot \left(k \nabla T \right) + Q \qquad (9)$$

where ρ is the density, C_p is the specific heat capacity, T is the absolute temperature, k is the thermal conductivity, ∇T is the temperature gradient, and Q is a heat source.

For fluids, additional contributions to heat transfer due to fluid motion are taken into account, specifically convection, viscous dissipation and pressure work:

$$\rho C_p \frac{\partial T}{\partial t} + \rho C_p \mathbf{u} \cdot \nabla T =$$
$$\alpha_p T \left(\frac{\partial p}{\partial t} + \mathbf{u} \cdot \nabla p \right) + \tau : \mathbf{S} + \nabla \cdot \left(k \nabla T \right) + Q \qquad (10)$$

where $\mathbf{u}$ is the velocity vector, α_p is the coefficient of thermal expansion, p is the absolute pressure, τ is the viscous stress tensor, and $\mathbf{S}$ is the strain-rate tensor.

Given equations (9) and (10), for solid materials the properties required for the computation are the thermal conductivity, the density and the specific heat capacity. These are shown in Table II. For fluid materials some of the aforementioned properties change with temperature and/or pressure so they were specified using interpolation functions. Additionally, for fluids the computation requires the dynamic viscosity and the ratio of specific heats to be specified.

To simulate convective heat transfer between the CSE and the surrounding air, a *Convective Heat Flux* boundary condition was assigned to all external surfaces of the CSE model:

$$q_0 = h \cdot \left(T_{ext} - T \right) \qquad (11)$$

where q_0 is the heat flux through a surface, h is the heat transfer coefficient, and T_{ext} is the temperature far away from the modeled domain which in this case is the same as the ambient temperature.

TABLE II
MATERIAL PROPERTIES FOR THERMAL COMPUTATION

Material	Thermal conductivity (W/m·K)	Density (kg/m³)	Heat capacity (J/kg·K)
Porcelain	2.00	2400	850
Cement	1.80	2300	880
XLPE	0.45	930	2300
Silicone rubber	0.25	1300	1500
EPR	0.20	1000	2000
Copper	390	8940	385
Aluminum	238	2700	900
Oil	0.1	$\rho_{oil}(T)$	$Cp_{oil}(T)$
Air	$k_{air}(T)$	$\rho_{air}(p, T)$	$Cp_{air}(T)$

Furthermore, radiative heat transfer was added to the model to account for radiation from the CSE external surfaces to the environment. This was achieved by assigning the *Surface-to-Ambient Radiation* boundary condition (12) to the external surfaces of the CSE model which coexists with a *Convective Heat Flux* boundary condition (11) for a combined contribution to heat transfer:

$$q_0 = \varepsilon \sigma \left(T_{amb}^4 - T^4 \right) \qquad (12)$$

where q_0 is the heat flux through a surface, ε is the surface emissivity, σ is the Stefan-Boltzmann constant, and T_{amb} is the ambient temperature.

For the CSE, heat is generated by resistive losses resulting from the flow of current in the conductor. To simulate this process, a *Heat Source* boundary condition was assigned to the conductor domains, which specifies that the heat source term Q to the right-hand side of equations (9) and (10) is equal to:

$$Q = Q_0 = \frac{R_{T-DC} I^2}{A_{con}} \qquad (13)$$

where Q_0 was specified as heat per unit volume, with I the current flowing through the conductor, A_{con} the cross-sectional area of the conductor (500 mm² for the CSE model), and R_{T-DC} the DC resistance of the conductor per meter specified as:

$$R_{T-DC} = R_{20-DC} \left[1 + \alpha \left(T - 20 \right) \right] \qquad (14)$$

where R_{20-DC} is the DC resistance of the conductor at 20°C and α is the temperature coefficient of electrical resistivity per Kelvin of the conductor material at 20°C.

To increase the accuracy of the computation, computational fluid dynamics (CFD) were coupled with the heat transfer physics to account for the flow of fluids (oil and air) present in the CSE model. Since the movement of fluids is not forced, the Reynolds number that characterizes the flow regime was estimated to be below the critical value defining the transition from laminar to turbulent flow. Hence, the *Laminar Flow* physics interface was used which solves the Navier-Stokes equations, specifically the conservation of momentum equation (15), the continuity equation for conservation of mass (16), and the conservation of energy equation (17):

$$\rho \frac{\partial \mathbf{u}}{\partial t} + \rho \left(\mathbf{u} \cdot \nabla \right) \mathbf{u} = -\nabla \cdot \left(p \mathbf{I} + \tau \right) + \mathbf{F} \qquad (15)$$

$$\frac{\partial \rho}{\partial t} + \nabla \cdot \left(\rho \mathbf{u} \right) = 0 \qquad (16)$$

$$\rho C_p \left[\frac{\partial T}{\partial t} + (\mathbf{u} \cdot \nabla) T \right] =$$

$$-(\nabla \cdot \mathbf{q}) + \tau : \mathbf{S} - \frac{T}{\rho} \frac{\partial \rho}{\partial T}\bigg|_p \left[\frac{\partial p}{\partial t} + (\mathbf{u} \cdot \nabla) p \right] + Q \tag{17}$$

where ρ is the density, $\mathbf{u}$ is the velocity vector, p is the pressure, τ is the viscous stress tensor, $\mathbf{F}$ is the volume force vector, $\mathbf{S}$ is the strain-rate tensor, and $\mathbf{q}$ is the heat flux vector.

The constitutive relation between stress and strain is also required, assuming all fluids in the model are Newtonian [20]:

$$\tau = 2\mu \mathbf{S} - \frac{2}{3} \mu (\nabla \cdot \mathbf{u}) \mathbf{I} \tag{18}$$

where μ is the dynamic viscosity.

The *Wall – No slip* boundary condition [21] was assigned to the internal surfaces of the CSE that come in contact with fluids. This condition defines that there is no flow across the aforementioned surfaces and no viscous stress in the tangential direction, and is therefore appropriate for modeling solid walls:

$$\mathbf{u} = 0 \tag{19}$$

To account for the influence of gravity on the flow of liquids, the *Gravity* feature was enabled in the *Laminar Flow* interface settings. This adds a volume force, $\mathbf{F_g}$, to the right-hand-side of equation (15):

$$\mathbf{F_g} = -\rho \mathbf{g} \tag{20}$$

where ρ is the density and $\mathbf{g}$ is the gravity vector.

Finally, the *Pressure Point Constraint* was used to specify the pressure level, p, for the liquids inside the CSE. Since the *Gravity* feature was enabled, the *compensate for hydrostatic pressure approximation* was also enabled which automatically adds the hydrostatic pressure, p_h, to the absolute pressure, p_0:

$$p = p_0 + p_h \tag{21}$$

with the hydrostatic pressure is specified as:

$$p_h = \rho \mathbf{g} \mathbf{h} \tag{22}$$

where $\mathbf{h}$ is the height of the fluid column.

The symmetry of the CSE along its longitudinal axis can be exploited to reduce the computational resource requirements for the model. For the thermal computation the two-dimensional (2D) model shown in Fig. 3 was used which was created by taking a cross-section of the electric field computation 3D model. The axis of symmetry is vertical (in Fig.3 it is shown horizontally for illustration purposes) so that the effect of
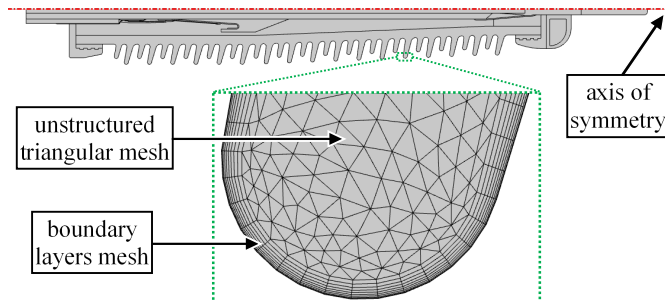

Fig. 3. 2D axi-symmetric CSE model used for the thermal simulation, demonstrating the combination of triangular and boundary layer mesh to ensure the accuracy of the computation.

gravity can be accounted for correctly. Special attention was given to the mesh due to the complex physics involved. Triangular mesh was used for the interior of most domains ensuring that at least two second-order elements were used per 90° arc [22]. The outer layers of the CSE geometry were modelled with a boundary layers mesh (Fig. 3) which increases the element density in the direction normal to the outer boundaries. This ensures the high quality of the mesh and consequently the accuracy of the computation.

C. Simulation Results and Analysis

For the electrostatics simulation, the voltage on the HV conductor and top ring boundaries was set to 76.2 kV, which is the nominal phase-to-ground voltage. The voltage on all other electrically conducting boundaries was set to 0 V. Fig. 4 shows the equipotential lines between HV and ground. Fig. 5 shows the electric field distribution and the maximum electric field magnitude and location reported by the electrostatic computation.

The simulation allows for the easy visualization of the effects of the electric field even inside the CSE. The geometric electric stress control employed reduces the axial stress caused by the discontinuity of the cable sheath. This is achieved by extending the sheath and gradually increasing the thickness of the insulation under it. The highest electric field magnitude of 6.9 kV/mm was observed near the end of the stress grading electrode closer to the sheath termination. Additionally, the highest electric field magnitude at the interface between solid and liquid dielectrics (stress cone and oil respectively), which has been shown to exhibit reduced breakdown strength [23], was computed to be 0.8 kV/mm. Finally, the simulation shows that the electric field magnitude attenuates rapidly when
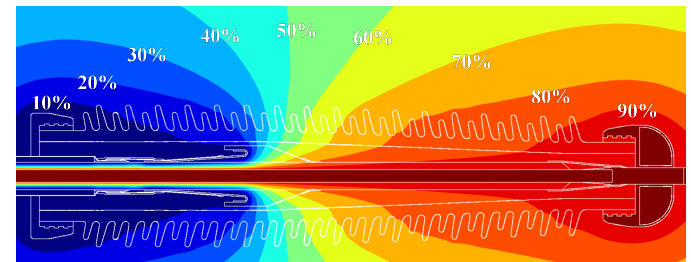

Fig. 4. Equipotential lines between HV and ground showing how the electric stress is reduced near the area of the sheath termination with the use of geometric stress control (stress cone).
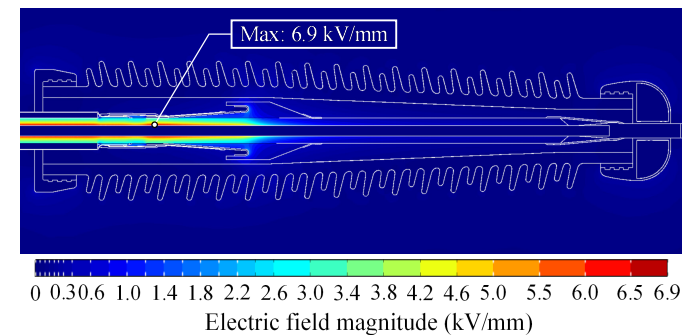

Fig. 5. Electric field plot of the CSE cross-section. The maximum electric-field magnitude based on the simulation results is 6.9 kV/mm, observed near the end of the stress grading electrode closer to the sheath termination.
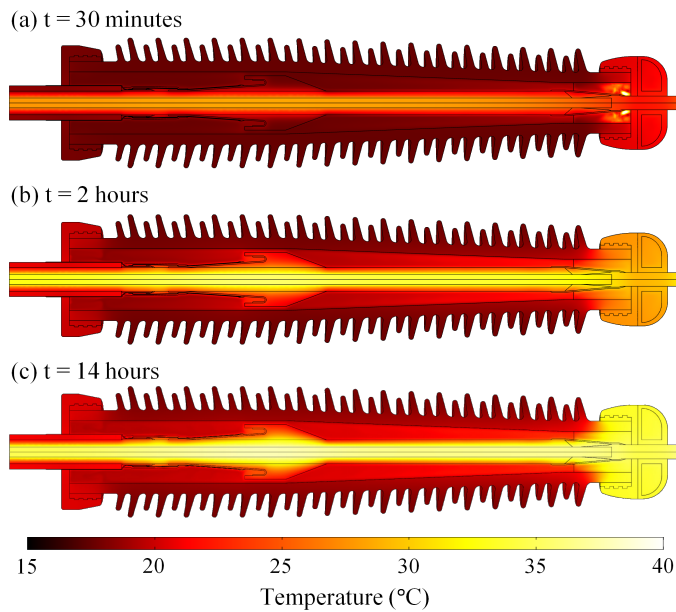
(a) t = 30 minutes

(b) t = 2 hours

(c) t = 14 hours

Fig. 6. Thermal computation heat plots of the CSE cross-section at time t = 30 min, 2 h and 14 h after energization.

moving away from the HV conductor. Outside of the CSE housing the observable electric field magnitude is less than 0.5 kV/mm.

For the thermal computation a time depended study was conducted. The ambient temperature was set to 17.5 °C to match that of the HV laboratory where testing was performed (reported in Section IV). For the same reason the current flowing through the HV conductor was set to 930 A. The temperature was computed in five-minute steps up to a total duration of 14 hours. Fig. 6 shows the results of the computation in the form of temperature plots at three time intervals, demonstrating how the CSE heats up. Fig. 7 shows how the temperature changes on the corona shield, on the tip of a shed in the middle of the porcelain housing, and on the bottom plate. The times required for the three components to reach thermal equilibrium are also indicated.

As expected, the hottest part of the model is the conductor, reaching temperatures of 42.4 °C. Despite the ability of the oil to circulate within the porcelain housing, its temperature is not uniform. Even when all other components reach thermal equilibrium, a temperature difference of 1.5 °C remains
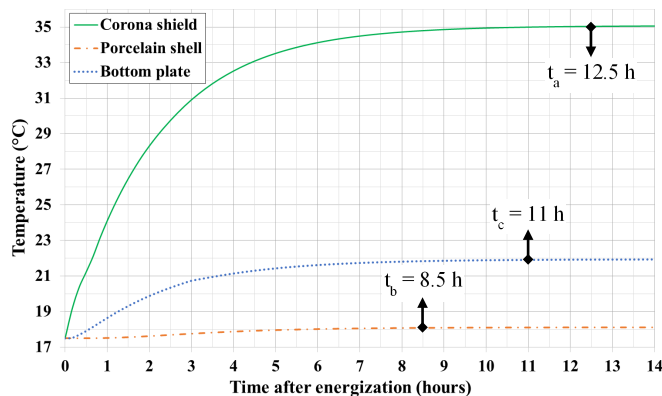

Fig. 7. Temperature change after energization and time required to reach thermal equilibrium for the corona shield (t_a), the porcelain shell (t_b), and the bottom plate (t_c), as reported by the thermal computation.

between the volume of oil below the stress cone and the volume above the stress cone. Furthermore, different components of the CSE reach thermal equilibrium at different times and different temperatures. The difference between the bottom plate and the top plate/corona shield is particularly pronounced with a difference of 12 °C. The aforementioned observations show that different parts of the CSE assembly are subjected to different thermal stresses and as a result they could be ageing at different rates. Lastly, it is important to note the temperature change of the porcelain housing. Starting from ambient before energization, it only rises by 1 °C to reach equilibrium. This could pose challenges for external thermal monitoring since the resolution of the instruments will have to be high enough to be able to distinguish between very small changes in temperature.

III. LIVE ELECTRIC FIELD TESTING

A. Electric Field Sensor

The electric field sensor shown in Fig. 8 is able to detect distortions to the electric field distribution surrounding a HV insulator caused by conductive or semi-conductive defects [24]. The construction of the sensor, consisting of a relatively small, U-shaped electric field probe flanked by two electrodes on either side, allows the sensor to be particularly sensitive to the axial component of the electric field [25].

The sensor is connected to a ski-guide assembly which ensures that the probe is always perpendicular to and at a constant distance from the longitudinal axis of the insulator. The assembly with the attached sensor is connected to a non-conductive, high dielectric strength hot-stick allowing the operator to slide the sensor along the insulator from a safe distance. A spring-loaded roller wheel activates the sensor every time it passes over the ridge of an insulator shed taking a measurement of the electric field magnitude. The data are transmitted to a paired Bluetooth-enabled device [26].

B. Test Setup

To measure the electric field magnitude and map the field distribution on the CSE, the test arrangement shown in Fig. 9 was assembled. The CSE was positioned on a steel structure resembling the structure that supports it when it is installed within a substation. A short cable section, with conductor cross-sectional area of 500 mm^2, was connected to the underside of the CSE and terminated. The free end of the cable was fitted
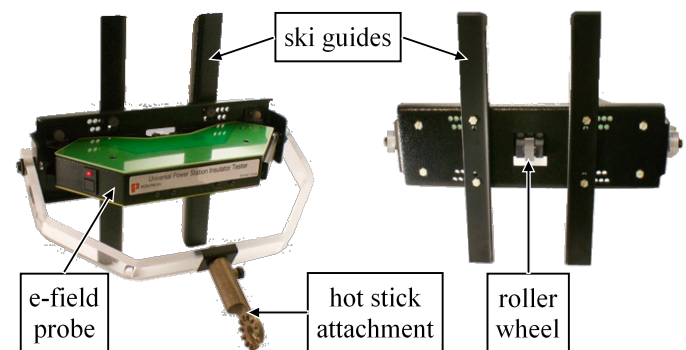

Fig. 8. Electric field sensor assembly showing the main components. The sensor takes a measurement of the axial component of the electric field magnitude when it passes over the ridge of an insulator shed.
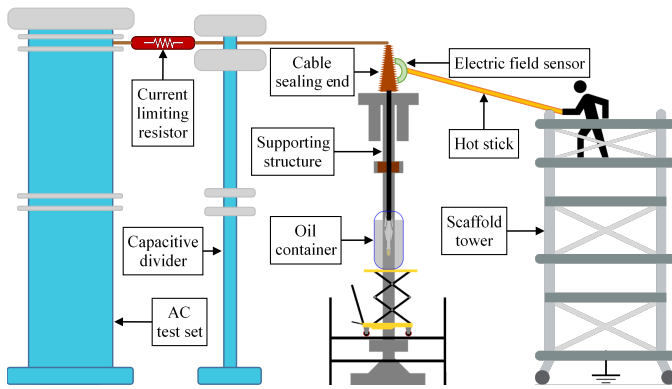
Fig. 9. Test setup for performing electric field measurements on a CSE. The HV test set energizes the top end of the CSE while the bottom end is connected to a short cable section terminated with a stress cone and placed in a plastic container filled with transformer oil.

with an electric field stress cone and placed in a plastic container filled with silicone transformer oil (Xiameter PMX-561 [27]). This was deemed necessary to minimize corona discharge and reduce the probability of flashover from the short cable section. The top end of the CSE was connected to an 800 kV AC test set via a HV capacitive divider.

To facilitate the testing, a scaffold tower was erected close to the CSE supporting structure. To minimize the risk of flashover, the safety clearance between the earthed scaffold and the nearest energized location was set to 2.5 m. This was more than five times the prohibition zone for live line work specified in BS EN 50191 [28]. For the same reason, the CSE was energized at 60 kV_{rms} which was below the nominal phase-to-ground voltage. To conduct the electric field measurement, a Live Line Engineer equipped with an arc flash suit operated the electric field sensor attached to a 3 m long hot stick (Fig. 10). The hot stick was connected to a leakage current detector with audible and visible alarm systems.

C. Results and Analysis

During the live test, four consecutive electric field measurements were performed on the CSE, yielding almost identical values. Due to the mode of operation of the sensor, the electric field was measured only when the sensor was passing over one of the seventeen large sheds of the CSE (Fig. 11). The simulation was adapted to reflect this as well as the position of
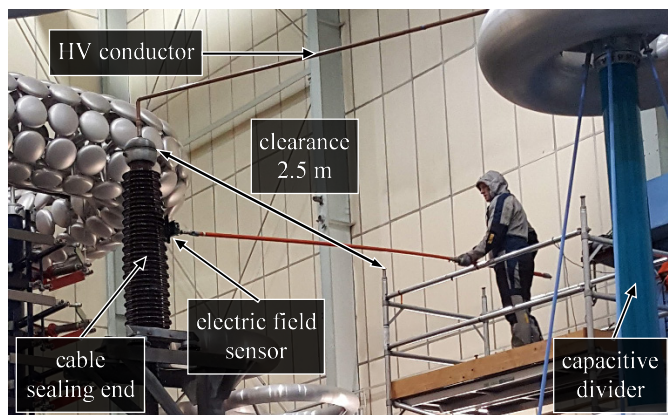

Fig. 10. Live-line engineer performing electric field measurement on an energized CSE in the HV laboratory. The electric field sensor is attached to 3 m long hot stick and transmits the data wirelessly to a paired device.

the electric field probe which is located at a distance of approximately 70 mm from the tip of the shed when a measurement is performed (due to the sensor assembly). Additionally, the simulation was configured to report only the axial component of the electric field, similarly to the sensor.

Fig. 12 shows the results from one of the measurements obtained with the electric field sensor. These are also compared with the corresponding results from the simulation. The profile of the computed electric field curve is very similar to that of the measurement. There is very close agreement of the values near the Ground and HV ends of the CSE with the difference being less than 0.005 kV/mm. On both curves the maximum electric field is observed at the location of the seventh shed (from the ground end) which is located directly on top of the stress cone. The maximum computed value was 0.059 kV/mm while the maximum measured value was 0.036 kV/mm.

The difference in electric field magnitude between simulation and measurement could provide an indication regarding the materials or the process involved in the construction of the cable termination. For example, the thickness of the insulating layers near the stress cone could be different (thicker in this case) than what was specified on the engineering drawings, i.e. more layers of insulating tape were used. Moreover, the difference could be attributed to the use of materials with higher dielectric constant than the ones originally specified e.g. for the stress cone.

IV. THERMAL TESTING

Infrared thermal imaging is a technique that allows the visualization of temperature variations and the measurement of the surface temperature of objects [29]. It is often used for condition monitoring and predictive maintenance.
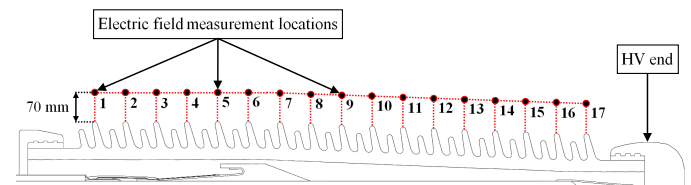

Fig. 11. Electric field measurement locations for the simulation. The field was computed 70 mm away from the tip of each of the 17 large sheds of the CSE to simulate the measurement taken by the electric field sensor.
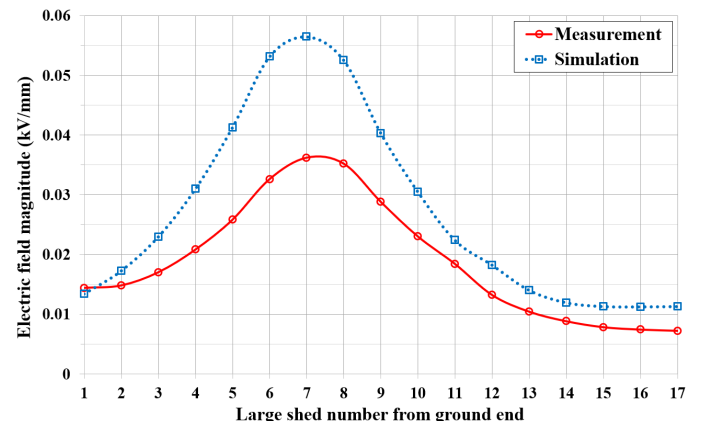

Fig. 12. Computed and measured electric field magnitude values taken at the tips of the 17 large sheds of the CSE.
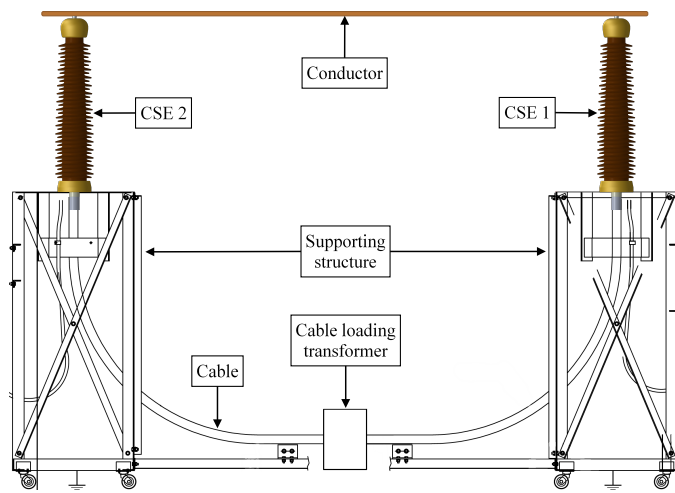
Fig. 13. Test loop for thermal testing. The cable loading transformer provides a current of 930 A to the loop consisting of two CSEs connected by HV busbar.

A. Test Setup

For testing the thermal performance of the CSE the rig in Fig. 13 was erected in the HV lab of the University of Manchester. It consists of a metallic support frame able to accommodate two CSEs, one on either side. One of the CSEs was filled with new oil while the other was filled with service-aged oil. At their underside the CSEs are connected by a short power cable which is terminated internally. At their top side, a HV busbar clamped on the connector stalks connects the two CSEs to complete the circuit. The cable passes through a cable loading transformer which is used to energize the test setup. The transformer was set to provide a current of 930 A. The FLIR T620 thermal camera was used to simultaneously record the surface temperatures of both CSEs. The ambient temperature was recorded to be 17.5 °C and remained constant for the duration of the test. Measurements were taken after the CSEs reached thermal equilibrium.

B. Results and Analysis

To construct the thermal profile, measurements were taken from two linear regions of interest (ROIs) along the porcelain housing of each CSE. The surface emissivity for the thermal images was set to 0.92, which is the emissivity of glazed porcelain and it is the same value that was used for the thermal simulation. Fig. 14 shows a thermal image of the two CSEs after reaching equilibrium and the ROIs used for the measurements. Fig. 15 shows the thermal profile of the CSEs and compares it to the one computed by the simulation over the same ROI.

Assuming that the simulation represents an ideal CSE, initial condition diagnosis can be performed for each of the two CSEs. CSE 1, which is the one filled with the service-aged oil, shows a temperature deviation from the ideal thermal profile at the lower end of the CSE (0.5 - 1.1 m) and near the location of the stress cone (1.6 - 2.2 m). The same behavior is not observed on CSE 2 with its temperature profile at the same areas being almost identical to the simulation. Although it would be difficult to determine the exact cause of the temperature profile deviation without looking inside the CSE housing, preliminary assumptions could be made regarding the condition of CSE 1.
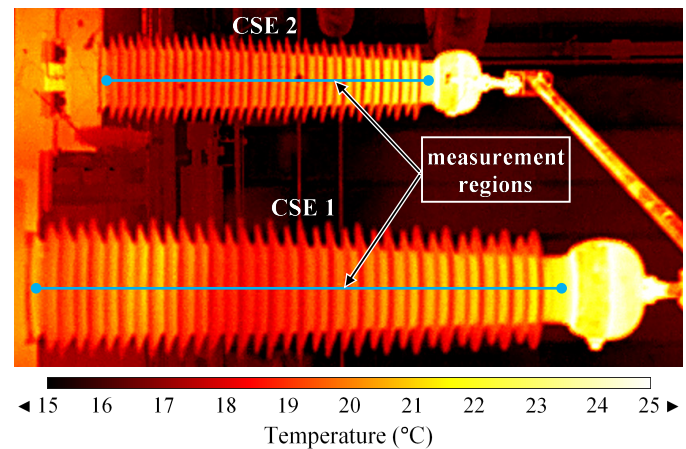

Fig. 14. Thermal imaging measurements on two 132 kV CSEs, with two linear regions of interest (ROIs) on the porcelain housing of each CSE.
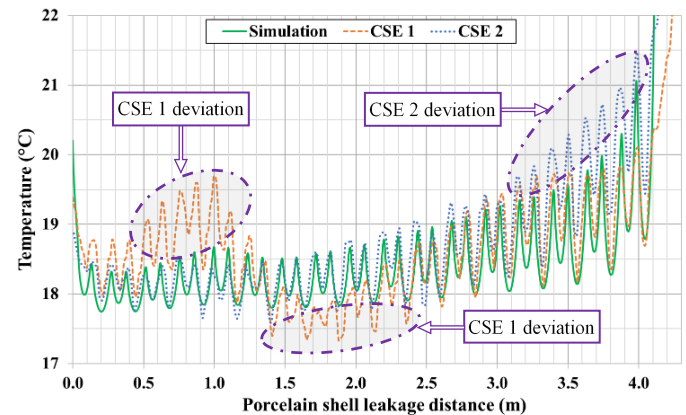

Fig. 15. Temperature profiles of the two CSEs obtained with thermal imaging and comparison with the simulation, highlighting the deviations from the expected behavior.

The deviation could be an indication that the cable termination for CSE 1 has been done slightly differently than what is specified on the engineering drawings, for example, using a different number of insulating tape layers. Also, the different properties of the service-aged oil, such as its viscosity, could be affecting its ability to circulate around the CSE in the same way that the new oil is able to, resulting is localized heating or cooling.

Furthermore, there is a deviation from the ideal profile at the top of CSE 2, near the HV end (3.2 - 4.0 m) which is not present in the simulation or the temperature profile of CSE 1. This could be indicating issues resulting in localized heating such as missing oil or high-resistance connection (HRC) between the HV stalk and the busbar. After visual inspection, the clamp connecting the CSE stalk to the busbar was found to be slightly loose, confirming the diagnosis of a HRC for CSE 2.

V. CONCLUSION

Good agreement has been obtained between the predictions from the electric field and thermal simulations and the measurements on a 132 kV oil-filled CSE. The electrostatic computation can provide information regarding the electric field distribution inside the CSE and help in identifying potential issues with the CSE design or the cable termination process. The thermal computation can reveal the temperature

differences between the various CSE components, which may result in non-uniform ageing, and provide information regarding the cooling efficiency of the liquid dielectric.

Combining the simulations with electric field and thermal imaging measurements, preliminary condition diagnosis can be performed without requiring the de-energization of the asset. Although the determination of the exact causes for the deviations are difficult to diagnose without additional testing, the method presented can provide the starting point for prioritizing maintenance operations.

REFERENCES

[1]   V. K. Agarwal, H. M. Banford, B. S. Bernstein, E. L. Brancato, R. A. Fouracre, G. C. Montanari, J. L. Parpal, J. N. Seguin, D. M. Ryder, and J. Tanaka, "The mysteries of multifactor ageing," *IEEE Electrical Insulation Magazine,* vol. 11, pp. 37-43, 1995.

[2]   K. Abdolall, G. L. Halldorson, and D. Green, "Condition assessment and failure modes of solid dielectric cables in perspective," *IEEE Transactions on Power Delivery,* vol. 17, pp. 18-24, 2002.

[3]   H. N. Nugamani and Channakeshava, "Investigations on the failure modes of XLPE cables and joints," *IEEE Transactions on Power Delivery,* vol. 13, pp. 706-711, 1998.

[4]   L. Cao and S. Grzybowski, "Accelerated aging study on 15 kV XLPE and EPR cables insulation caused by switching impulses," *IEEE Transactions on Dielectrics and Electrical Insulation,* vol. 22, pp. 2809-2817, 2015.

[5]   O. E. Gouda and A. Z. E. Dein, "Improving underground power distribution capacity using artificial backfill materials," *IET Generation, Transmission & Distribution,* vol. 9, pp. 2180-2187, 2015.

[6]   G. Mazzanti, "The combination of electro-thermal stress, load cycling and thermal transients and its effects on the life of high voltage ac cables," *IEEE Transactions on Dielectrics and Electrical Insulation,* vol. 16, pp. 1168-1179, 2009.

[7]   R. D. Rosevear, M. Choquette, M. Fairhurst, R. Garcia, H. J. Jorgensen, J. E. Larsen, B. Mampae, R. Mosier, A. Rakowska, H. Shigetsugu, S. Tricoli, and V. Waschk, "Update of Service Experience of HV Underground and Submarine Cable Systems," *CIGRÉ,* vol. Technical Brochure 379 - WG B1.10, 2009.

[8]   B. W. Tuinema, J. L. Rueda, L. v. d. Sluis, and M. A. M. M. v. d. Meijden, "Reliability of Transmission Links Consisting of Overhead Lines and Underground Cables," *IEEE Transactions on Power Delivery,* vol. 31, pp. 1251-1260, 2016.

[9]   Z. Iwata, B. Gregory, U. Amerphol, P. Argaut, K. Barber, H. Bergqvist, S. Koibuchi, J. P. Lamy, M. Laurant, P. Nyberg, B. Parmigiani, and M. R. Vermeulen, "Accessories for HV Cables with Extruded Insulation," *CIGRÉ,* vol. Technical Brochure 177 - WG 21.06, 2001.

[10] E. Bergin, C. Bradley, B. Mampaey, J. V. Rossum, S. Hvidsten, M. D. Lopez, C. Peacock, P. Wicht, W. Zenger, Y. Sudoh, R. Awad, N. Singh, X. Luo, D. S. Shin, F. Adamini, J. Beneteau, E. Dorison, and D. Jegust, "Guideline to Maintaining the Integrity of XLPE Cable Accessories," *CIGRÉ,* vol. Technical Brochure 560 - WG B1.29, p. 64, 2013.

[11] K. B. Liland, S. Hvidsten, G. Birkenes, F. Mauseth, G. A. Ward, and E. Bjerkan, "Development of a simple method for condition assessment of oil filled XLPE terminations," presented at the 8th International Conference on Insulated Power Cables, Jicable 2011, Versailles, France, 2011.

[12] F. Gahungu, J. Cardinaels, P. Streit, and D. Rollier, "Anti-explosion protection for HV porcelain & composite terminations," presented at the 6th International Conference on Insulated Power Cables, Jicable 2003, Versailles, France, 2003.

[13] M. M. A. Aziz and H. Riege, "Thermal Analysis of Cable Sealing Ends," *IEEE Transactions on Power Apparatus and Systems,* vol. PAS-99, pp. 829-832, 1980.

[14] R. C. Broughton, A. J. Oliver, D. R. Soulsby, P. L. Stephenson, W. Boone, and J. Kuiper, "Investigation of temperature and oil flow in EHV sealing ends," *IEE Proceedings C - Generation, Transmission and Distribution,* vol. 136, pp. 230-237, 1989.

[15] Y. O. Shaker, A. H. El-Hag, U. Patel, and S. H. Jayaram, "Thermal modeling of medium voltage cable terminations under square pulses," *IEEE Transactions on Dielectrics and Electrical Insulation,* vol. 21, pp. 932-939, 2014.

[16] J. Engelhardt, M. Floberg, R. Gear, and D. Orifice, "Model testing of an improved oil dielectric for high pressure oil-filled cable terminations," *IEEE Transactions on Power Delivery,* vol. 5, pp. 1225-1230, 1990.

[17] F. Mauseth, S. Hvidsten, and G. Birkenes, "Water ingress in high-voltage cross-linked polyethylene (XLPE) cable terminations," *IEEE Electrical Insulation Magazine,* vol. 28, pp. 24-31, 2012.

[18] COMSOL, "AC/DC Module User's Guide," vol. CM020101, ed: COMSOL, 2018.

[19] COMSOL, "Heat Transfer Module User's Guide," vol. CM020801, ed: COMSOL, 2018.

[20] G. G. Stokes, "On the Theories of the Internal Friction of Fluids in Motion, and of the Equilibrium and Motion of Elastic Solids," *Transactions of the Cambridge Philosophical Society,* vol. 8, pp. 287-319, 1845.

[21] G. K. Batchelor, *An Introduction to Fluid Dynamics.* Cambridge: Cambridge University Press, 2000.

[22] W. Frei. (2013). *Meshing Considerations for Linear Static Problems.* Available: http://www.uk.comsol.com/blogs/meshing-considerations-linear-static-problems/

[23] A. M. S. Katahoire, M. R. Raghuveer, and E. Kuffel, "Power Frequency and Impulse Voltage Breakdown along Silicone Oil/Xlpe Interface," *IEEE Transactions on Electrical Insulation,* vol. EI-16, pp. 97-104, 1981.

[24] F. Schmuck, I. Gutman, N. Mahatho, M. Perez, A. Phillips, A. Pigini, G. Pirovano, J. Seifert, M. R. Shariati, V. Sklenicka, W. Vosloo, and R. Wesley, "Assessment of in-service Composite Insulators by using Diagnostic Tools," *CIGRÉ,* vol. Technical Brochure 545 - WG B2.21, 2013.

[25] G. H. Vaillancourt, J. P. Bellerive, M. St-Jean, and C. Jean, "New live line tester for porcelain suspension insulators on high-voltage power lines," *IEEE Transactions on Power Delivery,* vol. 9, pp. 208-219, 1994.

[26] Positron Inc., "Positron Universal Substation Insulator Tester - Description and Operation Guide", Montréal, Canada2018.

[27] The Dow Chemical Company, "XIAMETER PMX-561 Transformer Fluid - Sales Specification", 2014.

[28] The British Standards Institution, "Erection and operation of electrical test equipment," *BS EN 50191:2010*, ed, 2010.

[29] M. Vollmer and K.-P. Mollmann, *Infrared Thermal Imaging.* Germany: Wiley-VCH, 2010.

Christos Zachariades was born in Athens, Greece, in 1984. He received the BEng (Hons) in electrical and electronic engineering, in 2009, the MSc in electrical power systems engineering, in 2010, and the PhD in electrical and electronic engineering, in 2014, from the University of Manchester, UK.

He was previously a Senior Test and Development Engineer with HVPD Ltd, UK, and a lecturer with the University of Manchester, UK, and is now a lecturer in Electrical Energy with the University of Liverpool, UK.

Dr. Zachariades is a Chartered Engineer (CEng) and a member of the Institution of Engineering and Technology (IET) as well as a member of the Cyprus Scientific and Technical Chamber (ETEK).

Vidyadhar Peesapati (M'10) was born in Edinburgh, UK, in 1980. He received the BEng in electrical and electronics engineering, in 2001, from the University of Madras, India, and the MSc in electrical power systems, in 2006, and the PhD in electrical and electronic engineering in 2010, from the University of Manchester, UK.

He is currently a Research Fellow at the University of Manchester, in the area of high voltage systems, asset management and condition monitoring.

Dr. Peesapati is a member of the IEEE and the IET.

Richard Gardner was born in Lincolnshire, UK, in 1983. He received the BEng (Hons) in mechanical engineering, in 2004, and an EngD in modal testing, in 2010, from The University of Manchester, UK.

Since then he has been a research associate working on high voltage systems in aerospace environments, an experimental officer, and now the high voltage laboratory manager at the National Grid Power Systems Research Centre at The University of Manchester, UK.

Oliver Cwikowski was born in in Ohio, USA, in 1989. He received the Meng (Hons) in electrical and electronic engineering, in 2012, and the PhD in electrical and electronic engineering, in 2016, from the University of Manchester, UK.

He is currently a Senior Innovation Engineer at National Grid Electricity Transmission where he leads underground transmission Innovation.

Dr. Cwikowski is a member of the IET.